ADVANCED PHOTONICS RESEARCH
Open Access
www.adpr-journal.com

LIPSS-Sticks: Laser Induced Double Self Organization Enhances the Broadband Light Absorption of TiO_2 Nanotube Arrays

Rakesh Arul, Junzhe Dong, M. Cather Simpson, and Wei Gao**

Sub-wavelength laser-induced periodic surface structures (LIPSS) created by ultrashort pulsed laser irradiation on the surface of titanium are used for the first time to template the electrochemical growth of titanium dioxide nanotube arrays, creating a combined structure we term LIPSS-Sticks. This is an example of a double self-organized process, as both LIPSS formation and electrochemical anodization involve spontaneous generation of order from initially nonordered precursors. LIPSS-Sticks have a 2× greater visible to near-infrared light (400–1400 nm) collection efficiency compared with flat titanium dioxide due to the enhanced light scattering from grating-like structures. The growth of nanostructures with time is modeled electrostatically to explain the features of a templated anodization process that differ from the usual anodization of flat surfaces. This new templated growth method using two complementary fabrication techniques is general and can also be applied to Cu, W, Fe, and Al oxide surfaces.

1. Introduction

In the pursuit of a sustainable future in the energy, transport and chemical industries, light-based technologies are leading the chase. The ability to store solar energy as fuel (e.g., hydrogen or methanol), to create chemical feedstock (e.g., nitrogen fixation[1]), or to remediate environmental pollutants through photocatalytic degradation holds the key to a "green" future. The first step in achieving these goals is the creation of a molecule/material that can efficiently absorb sunlight and turn solar energy into work in chemical reactions or electricity. The front-runner in the race for efficient photocatalysts are visible light-absorbing semiconductors. This study uses the classic transition metal oxide photocatalyst: TiO_2. Titanium dioxide has a long history in decomposing environmental pollutants,[2] water-splitting,[3,4] and as a support for dye-sensitized and perovskite photovoltaics,[5–7] but suffers from poor visible light absorption as it is a wide-bandgap semiconductor.

There exist two main paradigms to boost light collection efficiency and charge separation: 1) bandgap engineering through doping,[8] alloying,[9] defect control,[10] lattice strain, and heterostructuring;[11] and 2) morphology engineering to reduce recombination, increase crystallinity, and harvest light more effectively. Approaches such as thermal annealing introduce oxygen vacancies and increase visible light absorption,[10,12] but if too many defects are introduced, the electron–hole separation lifetime and the useful work extracted decreases, thus reducing overall photocatalytic reaction rates and efficiencies.[13] Here we attempt to circumvent this difficulty by nanostructuring the surface of the catalyst to more effectively harvest visible light while maintaining the elemental composition of the semiconductor. By multiple scattering of light in a nanostructured substrate, we increase the effective path length

R. Arul,[+] M. C. Simpson
The Photon Factory
The University of Auckland
Auckland, New Zealand
E-mail: c.simpson@auckland.ac.nz

R. Arul, M. C. Simpson
The MacDiarmid Institute for Advanced Materials and Nanotechonology
Wellington Central, Wellington 6011, New Zealand

The ORCID identification number(s) for the author(s) of this article can be found under https://doi.org/10.1002/adpr.202000133.

[+]Present address: NanoPhotonics Centre, Cavendish Laboratories, University of Cambridge, J. Thomson Avenue, Cambridge CB3 0HE, UK

DOI: 10.1002/adpr.202000133

R. Arul, M. C. Simpson
The Dodd Walls Centre for Quantum and Photonic Technologies
Dunedin, New Zealand

R. Arul, M. C. Simpson
School of Chemical Sciences
the University of Auckland
Auckland, New Zealand

R. Arul, M. C. Simpson
Department of Physics
The University of Auckland
Auckland, New Zealand

R. Arul, J. Dong, W. Gao
Department of Chemical and Materials Engineering
The University of Auckland
Auckland, New Zealand
E-mail: w.gao@auckland.ac.nz

of light in the material, enabling a greater absorption of light even if the absorption coefficient of a material is small.

Light trapping in poorly absorbing substrates is a well-studied topic,[14,15] and several approaches have been used including photonic crystals, gratings diffracting light at oblique angles, planar back-reflectors, and surface nanostructures which allow incident light to couple into quasi-guided modes in a thin film. Prior work[16,17] has suggested that optimum light-trapping efficiency is achieved between the extremes of a random Lambertian scattering surface (exciting a large number of diffraction orders resulting in a $4n^2$ increase in path length[18] where n is the medium's refractive index) and a grating-like surface (exciting few grating orders).

High aspect ratio metal-oxide nanotubes can be produced using electrochemical anodization of metallic sheets;[19] and nanotube size, wall thickness, and array symmetry can be controlled by the anode voltage, anodization time, and electrolyte. This self-organized process creates hexagonally periodic nanotube arrays by balancing two reactions: metal oxidation to form an oxide and chemical dissolution of the oxide.[20] Indeed, the confluence of all these microscopic effects produces a large-scale organized structure which is a paradigm of self-organization,[21] similar to Turing patterns,[22] and their true description is still an active area of research.[23,24] Similarly, laser-induced periodic surface structures (LIPSS)[25,26] are sub-wavelength self-organized structures that can be patterned by an ultrashort pulsed laser on a range of different metals, polymers, and dielectrics.[27] LIPSS surface ripples have a periodicity that is smaller than the wavelength of the laser, with an orientation depending on the polarization.[28,29]

The sub-wavelength periodicity of LIPSS formation on metallic surfaces[30] has two main explanations: the interference model and the self-organization model. The interference model takes a "light-centric" view that the interference of incident light and a surface-scattered wave exciting the surface plasmon polariton of a metallic surface[28] creates a local intensity modulation that results in a ripple morphology.[31,32] The self-organization model takes a "material-centric" view that the absorbed laser energy induces a softening and instability of the metallic surface due to melting,[33] in a similar vein to ion-beam-induced structures.[34]

By patterning the surface of Ti metal with LIPSS prior to electrochemical anodization (**Figure 1**), we fabricated arrays of TiO_2 nanotubes that organized into ripples, thus acting as a grating to enhance the trapping of visible light.[35–37] The ability to pattern LIPSS on Ti has been previously reported.[38–42] However, we show below the first-known case of LIPSS being used to template the growth of anodic TiO_2 nanotubes in a grating structure, and as a templating technique for nanostructured metal oxide growth in general, which we term "LIPSS-Sticks".

2. Results and Discussion

2.1. Increased Visible to Near-Infrared Light Harvesting Efficiency of LIPSS-Sticks

The laser fluence and number of overlapped laser pulses was varied (optimization results shown in S1, Supporting Information) to determine the periodicity of LIPSS produced

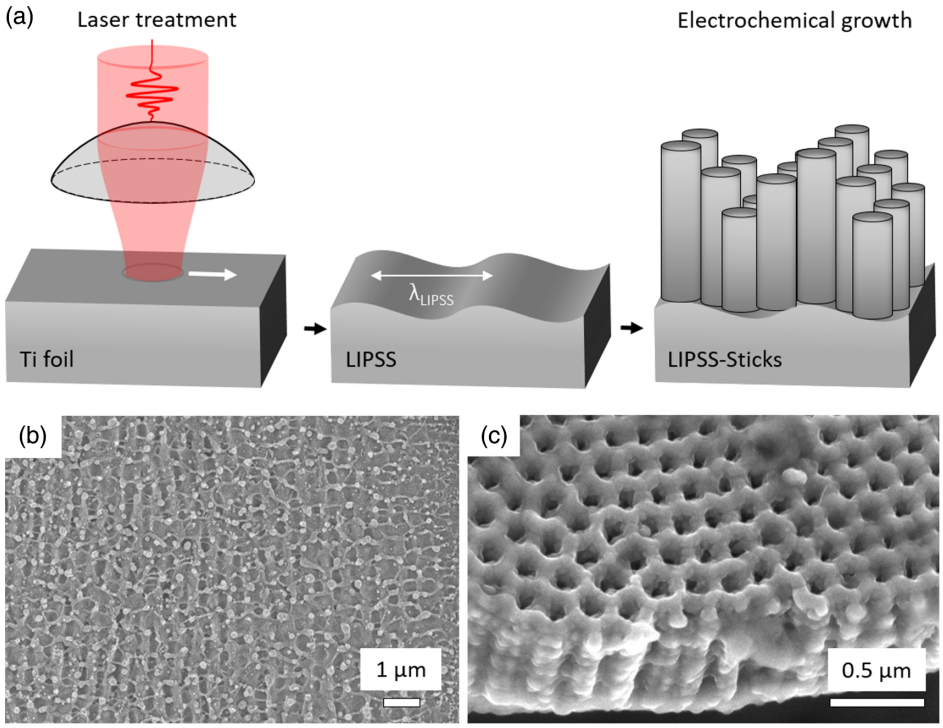

Figure 1. Double self-organization: a) Schematic of self-organized LIPSS and subsequent self-organized growth of nanotubes. Femtosecond pulsed laser irradiation is focused through a lens to treat the surface of Ti metal foil and create self-organized surface ripples (LIPSS) which are used as templates for self-organized electrochemical growth of TiO_2 nanotube arrays. SEM images of b) LIPSS structure on titanium metal substrate, and c) TiO_2 nanotube arrays electrochemically grown on flat/non-laser-treated titanium metal.

with femtosecond pulsed laser treatment (800 nm, 1 kHz, 130 fs) on flat electropolished Ti metal foil. We reproducibly fabricated sub-wavelength structures with periodicity between 250 and 650 nm using a mask to define a 50 μm × 50 μm spot size, tuned the incident power using a laser attenuator, and varied the number of overlapped pulses by changing the translation speed of the stage under the laser. The morphology of the resulting LIPSS was imaged with a scanning electron microscope (SEM). The laser conditions corresponding to a spatial periodicity of 350 and 500 nm (0.105 J cm^{-2}, 250 overlapped pulses; and 0.087 J cm^{-2}, 50 overlapped pulses, respectively) were chosen for further templating experiments and large samples (2 cm × 2 cm) were made for optical measurement by rastering the laser over the Ti surface. The laser fluences chosen were below the ablation threshold fluence of Ti metal (0.16 J cm^{-2} for 50 pulses and 0.12 J cm^{-2} for 250 pulses at 800 nm and 110 fs pulse duration[43]), hence we only perform surface structuring without more extensive laser ablation. The initial laser patterned periodicity of the LIPSS on Ti foil will henceforth be used to label both the substrate types as $\lambda_{LIPSS} = 350$ nm and $\lambda_{LIPSS} = 500$ nm.

Figure 2 shows the growth of the LIPSS structured surface under electrochemical anodization with time. Initially, the laser-treated surface showed only grating-like ripples from the LIPSS. After 3 h of anodization, TiO_2 nanotubes with an initial periodicity imprinted by the laser treatment were formed. After 7 h, the rippled surface structure was destroyed as the nanotubes grew too long and were etched away, collapsing under their own weight.[44] The $\lambda_{LIPSS} \approx 500$ nm sample displays inhomogeneity in the LIPSS structure over the 5–10 μm scale (Figure 2b T = 0 h) due to operation in an unstable LIPSS formation regime which amplifies inhomogeneity in the beam profile. This inhomogeneity is reduced by rastering the beam across the sample (Section S6, Supporting Information) and is also minimized once the nanotubes form at >3 h (Figure 2b $T = 3$ h).

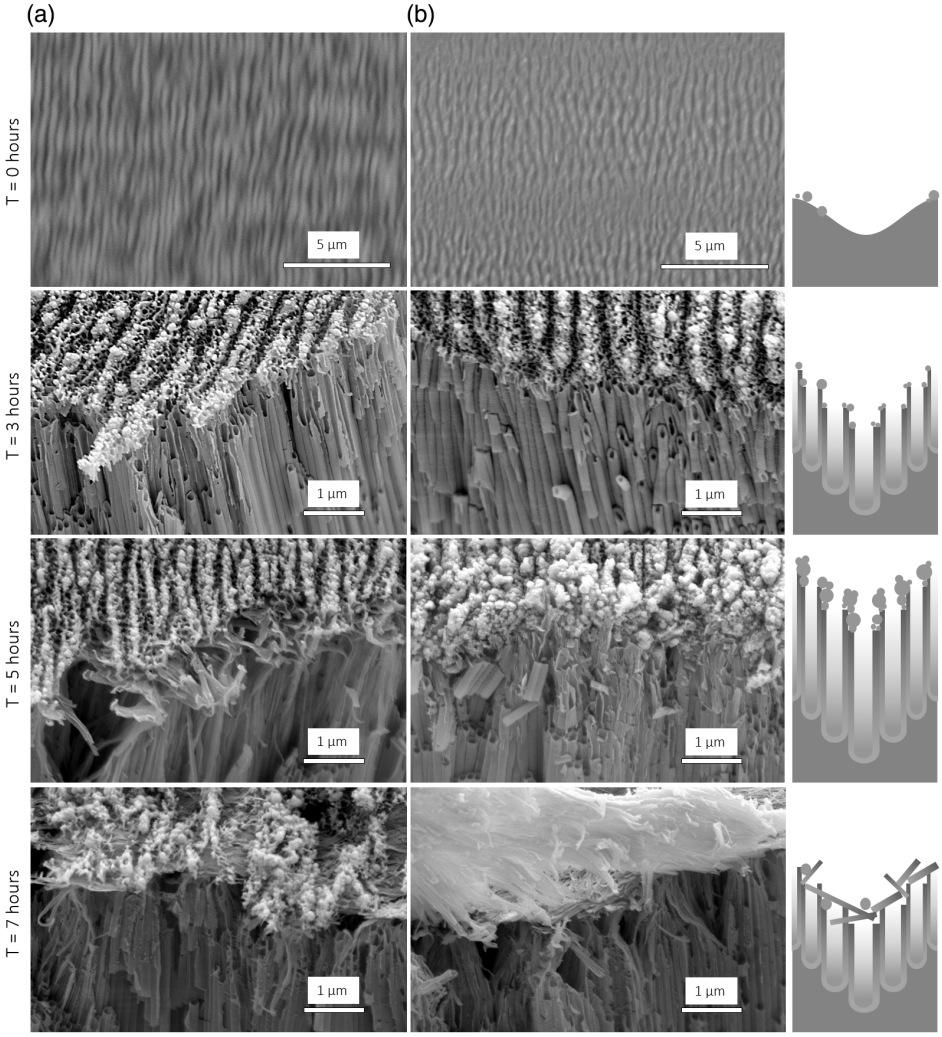

Figure 2. LIPSS-Sticks hierarchical nanostructure composed of submicron ripples on oxide nanotubes. Evolution with time over 7 h is shown for electrochemical anodization of samples with initial LIPSS periods: a) $\lambda_{LIPSS} = 350$ nm and b) $\lambda_{LIPSS} = 500$ nm. Cross-sections were obtained by brittle fracture/delamination of the oxide film and tilted (45°) imaging in the SEM. Right: Schematic of the cross-sectional morphology at each corresponding anodization time.

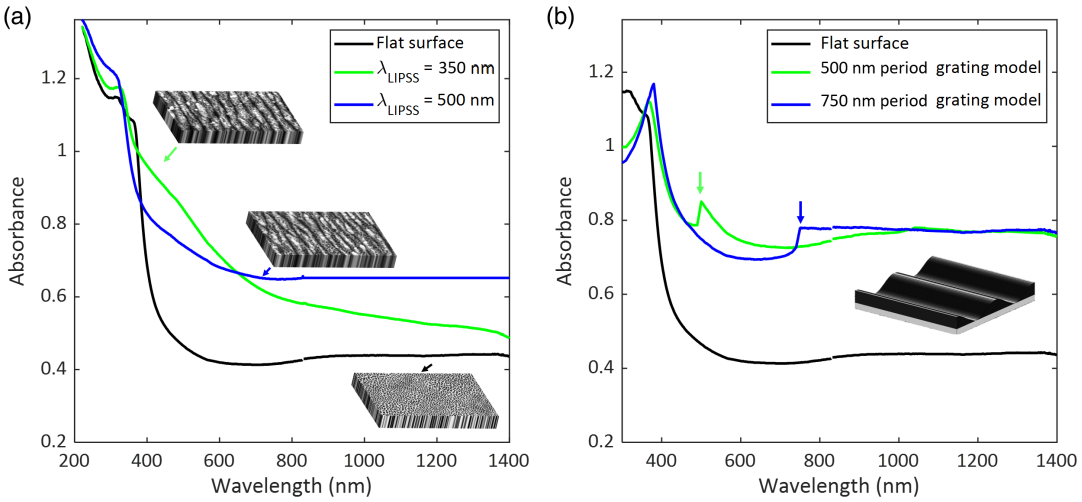

Figure 3. Increased visible to near-infrared light extinction of the LIPSS-Sticks: a) Diffuse reflectance spectra for as-anodized samples (flat surface) and LIPSS-Sticks samples with initial LIPSS periodicities of $\lambda_{LIPSS} = 350$ and 500 nm after 3 h of anodization, normalized to extinction <300 nm due to interband transitions. Inset shows the surface morphology. b) Simulated extinction of grating structures of TiO_2 with the same periodicity as the LIPSS-Sticks (expanded to 500 and 750 nm after anodization compared with the initial LIPSS period).

The LIPSS-Stick substrates for $\lambda_{LIPSS} = 350$ nm and $\lambda_{LIPSS} = 500$ nm initial LIPSS periodicities showed increased light extinction relative to the flat nonlaser-processed TiO_2 nanotube array (**Figure 3**a). The diffuse reflectance of these films was measured using a commercial UV–vis spectrometer with an integrating sphere attachment (Section S7, Supporting Information), and normalized to the extinction in the UV region (<300 nm) which is due to interband transitions in TiO_2 and shared by all three samples. Flat TiO_2 already shows an appreciable visible-NIR light absorption beyond its band edge due to the scattering of the nanostructures on the ≈10 µm thick film and sub-bandgap defect absorption. Light extinction is increased over a large wavelength range, from the visible (near the band-edge of TiO_2) to the near-infrared (deep within the bandgap energy of TiO_2).

We further characterized the chemical structure of the entire surface using X-ray photoelectron spectroscopy (XPS), which yielded very similar spectra for the unmodified anodized TiO_2 and the LIPSS-Sticks surfaces (**Figure 4**c). XPS survey spectra (Section S5, Supporting Information) show that the Ti:O atomic ratios do not change significantly between the flat Ti surface (Ti:O = 1:2.8), the $\lambda_{LIPSS} = 350$ nm (Ti:O = 1:2.7), and the $\lambda_{LIPSS} = 500$ nm (Ti:O = 1:2.9) LIPSS-Sticks surfaces after 3 h of anodization. The only change is a difference in fluorine content (6% on the flat surface, 8% in the $\lambda_{LIPSS} = 350$ nm, and no observable fluorine in the $\lambda_{LIPSS} = 500$ nm). Detailed fitting of the XPS spectra can be found in Section S5, Supporting Information, and show no significant change in binding energy positions ($2p_{3/2}$ peak at 458.8 eV) or peak ratios. As the chemical structure of the TiO_2 nanotubes are very similar with and without

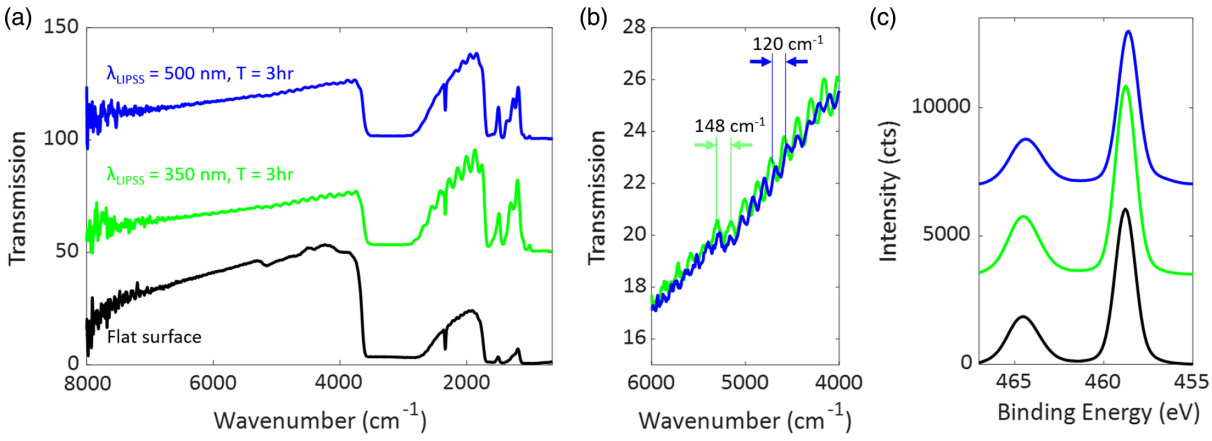

Figure 4. Chemical characterization of LIPSS-Sticks films a) Infrared (FTIR) reflectance spectrum of as-anodized samples (flat surface, black) and LIPSS-Sticks samples with initial LIPSS periodicities of $\lambda_{LIPSS} = 350$ nm (green) and 500 nm (blue) at 3 h of anodization. b) FTIR spectrum of $\lambda_{LIPSS} = 350$ nm (3 and 10 h anodization) and 500 nm (3 h of anodization) with Fabry–Perot thin-film interference fringes' free spectral range indicated. c) Ti 2*p* XPS of flat TiO_2 as-anodized surface and LIPSS-Sticks samples at 3 h of anodization.

LIPSS templating, the increased extinction must be due to the increased light scattering of the hierarchical LIPSS-Sticks structure, as opposed to an increased density of sub-bandgap defect states.[10] The nanostructured material scatters the light and thereby increases the interaction between light and the material.

To a first approximation, we can model the increased light extinction by considering the optical scattering of a grating structure composed of unidirectional sinusoidal surface ripples. The simulated geometry has a peak-to-trough depth of 100 nm and an expanded period of 500 nm and 750 nm, due to the growth of nanotubes widening the LIPSS-Sticks's spatial period (Figure 2). The scattering of the grating at normal incidence was computed using GD-Calc,[45] which solves Maxwell's equations using the rigorous coupled wave method.[46] The wavelength-dependent complex dielectric function of TiO_2 was taken from ref. [47], with a refractive index around 2.5.[48] The average extinction efficiency (ratio of intensity absorbed and scattered to the incident intensity) was calculated for unpolarized (averaged *s*- and *p*- polarization) electromagnetic waves irradiating the surface of the grating, and up to 10 diffraction orders were computed.

The grating's predicted extinction spectrum (Figure 3b) exhibited generally increased broadband light extinction compared to the flat substrate. The increased visible-light extinction between 400–680 nm of the substrate with a 350 nm LIPSS period was also reproduced. However, the grating simulation shows the presence of sharp diffraction orders, which are not seen in the measured sample due to the disordered distribution of the 100 nm nanotubes that was not included in our simplified model. Due to the roughness of the surface, the higher diffraction orders are not as distinct, and only the first diffraction order survives, which explains the higher visible wavelength extinction of the $\lambda_{LIPSS} = 350$ nm substrate and the higher near-infrared wavelength extinction of the $\lambda_{LIPSS} = 500$ nm substrate. This is only an approximate description, and a more complete picture of light scattering should account for the nanotube structure as well as the surface nanoparticles. Furthermore, the measurements were performed inside a $BaSO_4$ referenced integrating sphere, further introducing complications due to multiple scattering which are not easily accounted for.

In a grating structure, light absorption is reduced by diffraction into lower order diffraction modes, due to the small diffraction angle not exceeding the total internal reflection angle of the structure (24° for a TiO_2–air interface), and thus light only performs one pass through the structure, not the multiple passes needed to enhance absorption. In our structure, the majority of scattering is into the lower diffraction orders. However, the presence of surface disorder and scattering means that the near-normal incidence light, although lower than the total internal reflection angle, ends up being scattered into the sample again. The disorder also broadens the spectral range over which enhanced absorption occurs, and reduces the angle dependence of the grating.[17]

Thin-film interference effects were not considered in the visible regime, as the thickness of the anodized TiO_2 films were >10 μm, hence the fundamental Fabry–Perot mode was in the mid-infrared (Figure 4a), and higher-order modes in the visible regime were suppressed due to destructive interference and scattering on the rough top surface ripples. The Fourier-transform infrared (FTIR) spectrum in Figure 4a is dominated by contributions due to adsorbed water at 3400 and 1630 cm^{-1}. Peaks due to the Ti–O vibrations are saturated due to the strongly adsorbing surface hydroxide and water layers below 1000 cm^{-1}. The ripples in the FTIR spectrum are due to the Fabry–Perot interference effects (Figure 4b), where the ripples have a periodicity/free-spectral range of $c/2nL$ where c is the speed of light, $n \approx 2.5$ is the refractive index of TiO_2, and L is the thickness of the TiO_2 layer. A free-spectral range of 148 and 120 cm^{-1} yielded similar film thicknesses of 13 and 17 μm for LIPSS-Sticks with $\lambda_{LIPSS} = 350$ and 500 nm at 3 h of anodization, respectively.

2.2. Growth Morphology and Dynamics of LIPSS-Sticks

The dynamics of self-organization were explored by stopping anodization at 1, 3, 5, and 7 h and measurement under the SEM. All LIPSS-patterned surfaces show a markedly different morphology than the control or non-laser-treated anodized TiO_2 (**Figure 5**). LIPSS-structuring of Ti often leaves surface Ti oxides and redeposited oxide nanoparticles, as seen in Figure 5a, which is expected as we are in the thermochemical LIPSS regime under ambient conditions.[27] Anodized TiO_2 without laser treatment has an irregular nanotube structure with an average nanotube size of 120 nm from 1 to 5 h, and a nanoforest geometry forming at 7 h due to the etching and collapse of nanotube walls.[49]

For the LIPSS structured Ti surface anodization, the initial rippled nanostructure is preserved in the electrochemical growth. The preservation of this structure is unexpected as computational studies,[50] and linear stability analysis of the oxide interface[21] suggests there is a special spatial period corresponding to the nanotube spacing that is exponentially amplified, and all other amplitudes are amplified to a lesser extent or are suppressed. Hence, the preservation of the ripples up to 5 h of growth has to be attributed to second-order effects such as the prestress introduced to the metal film or initial oxide layer produced due to LIPSS, which will be the subject of future study.

After 1 h of LIPSS-Sticks growth, the self-organized nanotube structure begins to form for both $\lambda_{LIPSS} = 350$ and 500 nm surfaces (**Figure 6** at high magnification, and **Figure 7** at low magnification). The initial periodicity due to the LIPSS patterning is retained and results in a wave-like modulation of the nanotubes' surface profile with a larger period of 300 and 600 nm (white arrows in Figure 7 at $T = 1$ h). The increase in spatial period is due to the growth of nanotube walls with a typical thickness of 20 nm. Nanotube diameters within the valleys of the ripple are larger than those at the hills (red circles in Figure 6). This observation can be explained by the enhanced electric field within the valleys, causing a larger valley nanotube size than at the crests. This is analysed by computational modeling in the following section. The nanotube wall thicknesses remain constant between the two patterns, which indicates that the LIPSS structures act to modify the overall surface relief without altering the shape of the nanotube walls.

After 3 h of anodization, the nanotube walls become thicker and the oxide layer itself increases in cross-sectional thickness to ≈20 μm. The periodicity remains similar to that at 1 h anodization. Nanoparticle deposits begin to grow on the surface of

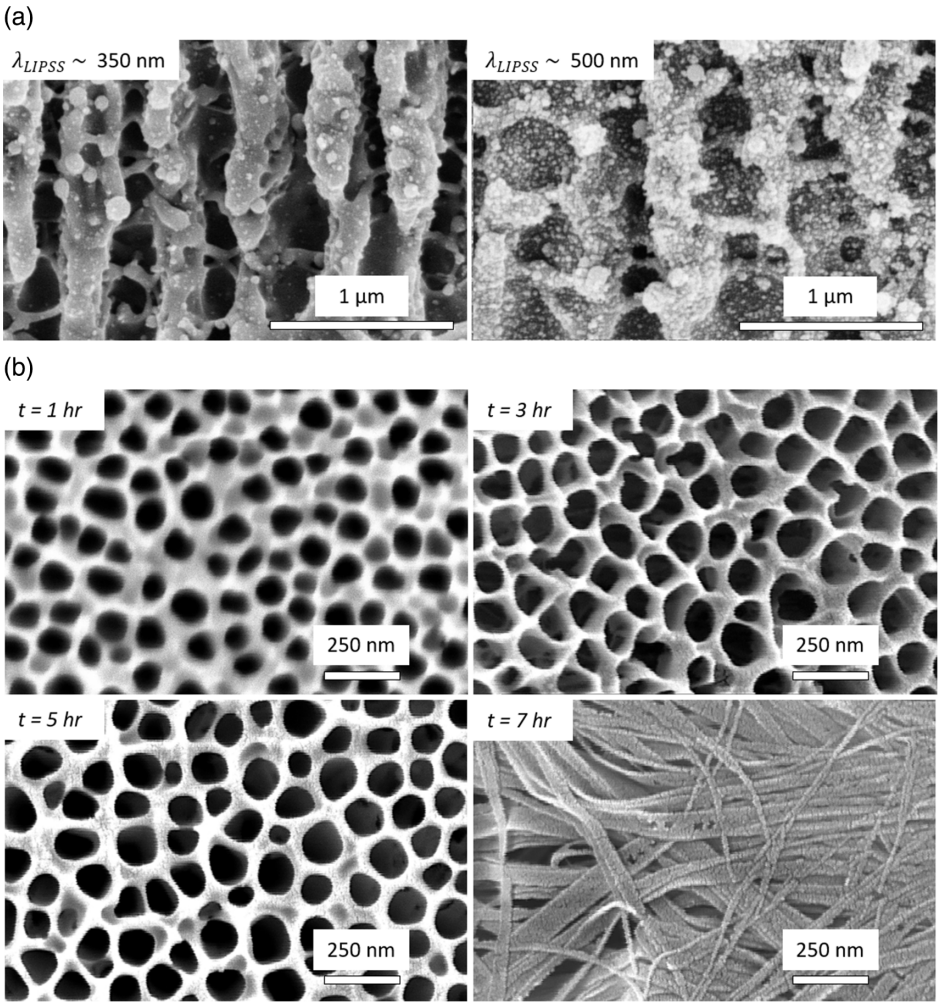

Figure 5. Surface morphology: a) LIPSSs on Ti, and b) anodized TiO_2 surface without surface modification. Anodization time is listed.

both samples, although more prominently in $\lambda_{\mathrm{LIPSS}} = 500\,\mathrm{nm}$ sample, and more prominently on the crests than the valleys. We suggest that these nanoparticles are nucleated from the spheroidal ejected material created during the LIPSS patterning process (Figure 5a). These then grow into the larger deposits seen in Figure 6. The cross-sectional structure in Figure 2 shows that the nanotube structure remains intact through the bulk of the material. The nanoparticles on the LIPSS-patterned TiO_2 nanotube surface were imaged at 20 kV under the SEM and the EDX spectrum shown in Section S4, Supporting Information. The EDX atomic percentage indicates that the structures are primarily defective titania, with an elemental formula of approximately $TiO_{1.4}$. There are traces of F and C from the fluoride containing organic electrolyte (ethylene glycol).

As the anodization time increases to 5 h, the nanoparticle deposits continue to grow in size and the layer thickness increases to ≈40 µm. In some areas, the nanoparticle deposits grow over the top of the nanotubes, especially in the hills of the ripples, and the nanotube walls begin to be further etched and display ribbon-like structures (Figure 2). Nanotube cross-sections are much better developed for the $\lambda_{\mathrm{LIPSS}} = 500\,\mathrm{nm}$ sample. The additional surface area that results from the surface-nanoparticles have the potential to be beneficial to its photocatalytic properties.

At 7 h of anodization, the nanoforest geometry forms on $\lambda_{\mathrm{LIPSS}} = 350\,\mathrm{nm}$ patterned structure, while the 500 nm patterned surface retains its nanotubes, except on the patterned structure's edges. The formation of the nanoforest is expected, as the non-laser-treated Ti foil has a nanoforest geometry at 7 h of anodization. In the cross-sectional images in Figure 2, we can see how the edges of the nanotubes become etched and collapse down to the nanoforest of nanotube walls on the surface forming a thick mat. Further cross-sectional images can be seen in Section S6, Supporting Information.

2.3. Electrostatic Simulations of Nanotube Growth

To understand the nanotube growth, we develop a simple electrostatic model simulating the static electric-field distribution and the current density within specific predetermined geometries of LIPSS-patterned Ti foil prior to and during anodization. We numerically solve the 2D Poisson's equation (Equation (1))

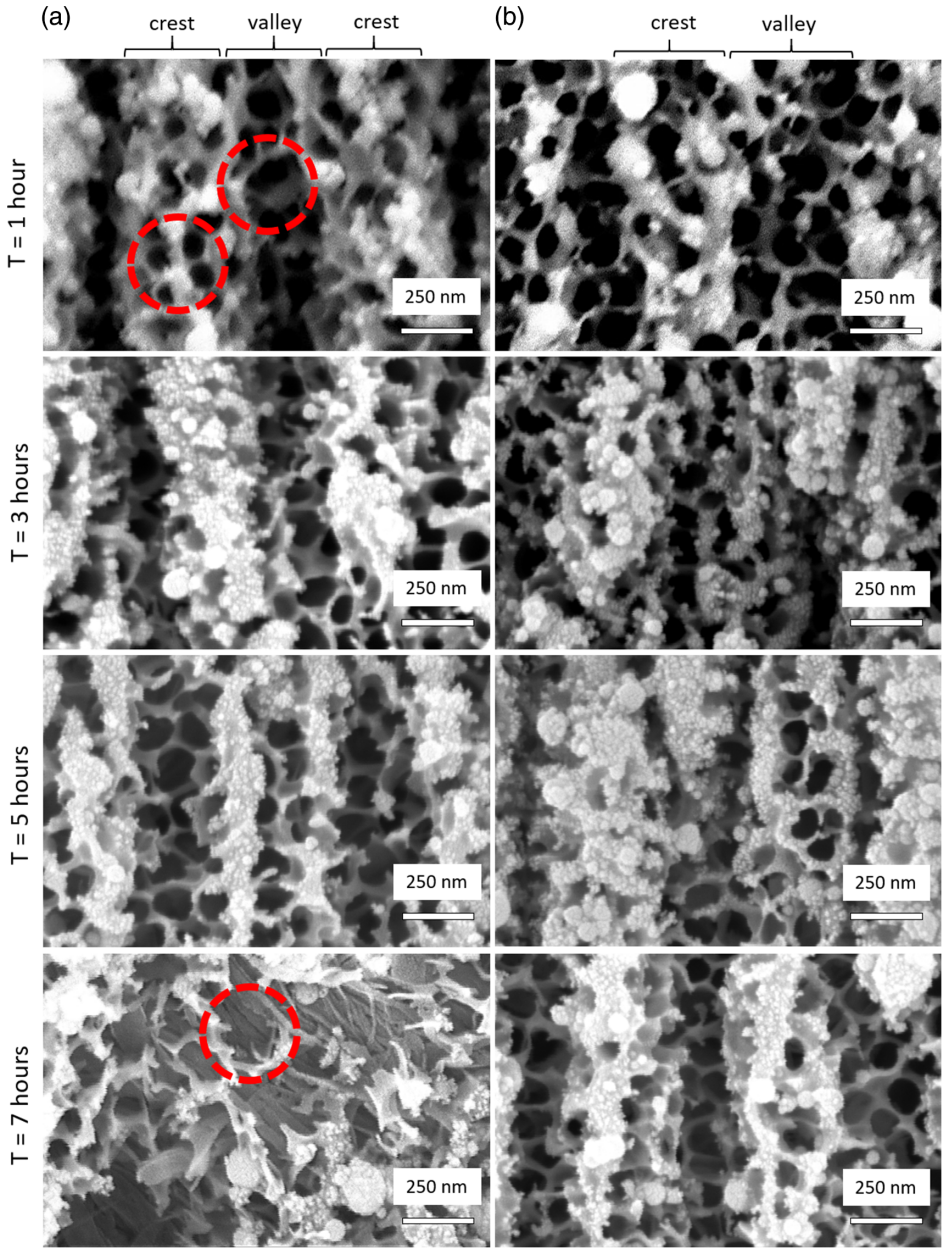

Figure 6. Time evolution of the surface morphology of LIPSS-Sticks with initial LIPSS periods: a) $\lambda_{LIPSS} = 350$ nm and b) $\lambda_{LIPSS} = 500$ nm. Red circles indicate the different nanotube geometries in the valleys versus crests of the structure, and the nanoforest formed after 7 h of anodization.

for the electrostatic potential within the TiO_2 film using the finite element method in COMSOL Multiphysics. We only consider TiO_2 and not the electrolyte as most of the potential drop from the electrodes occurs over the insulating oxide layer and not the conductive electrolyte.[51] In Equation (1), ∇ is the partial derivative operator, ε_0 is the permittivity of vacuum, ε_r is the relative static permittivity of TiO_2, V is the electric potential, and ρ is the space-charge density.

$$-\nabla \cdot (\varepsilon_0 \varepsilon_r \nabla V) = \rho \tag{1}$$

The boundary conditions are set such that the initial space-charge density $\rho = 0$, the bottom metal–oxide interface has a potential equal to the applied voltage of 60 V, and the top oxide-electrolyte interface is assumed to be at 0 V. Periodic boundary conditions are imposed on the edges of the oxide layer. The detailed material and geometric parameters used are listed in Table S2, Supporting Information. The electrostatic field solutions for different geometries, corresponding to the evolving morphology of the nanotube array, are plotted in **Figure 8**. The current density j can be extracted from the solution for

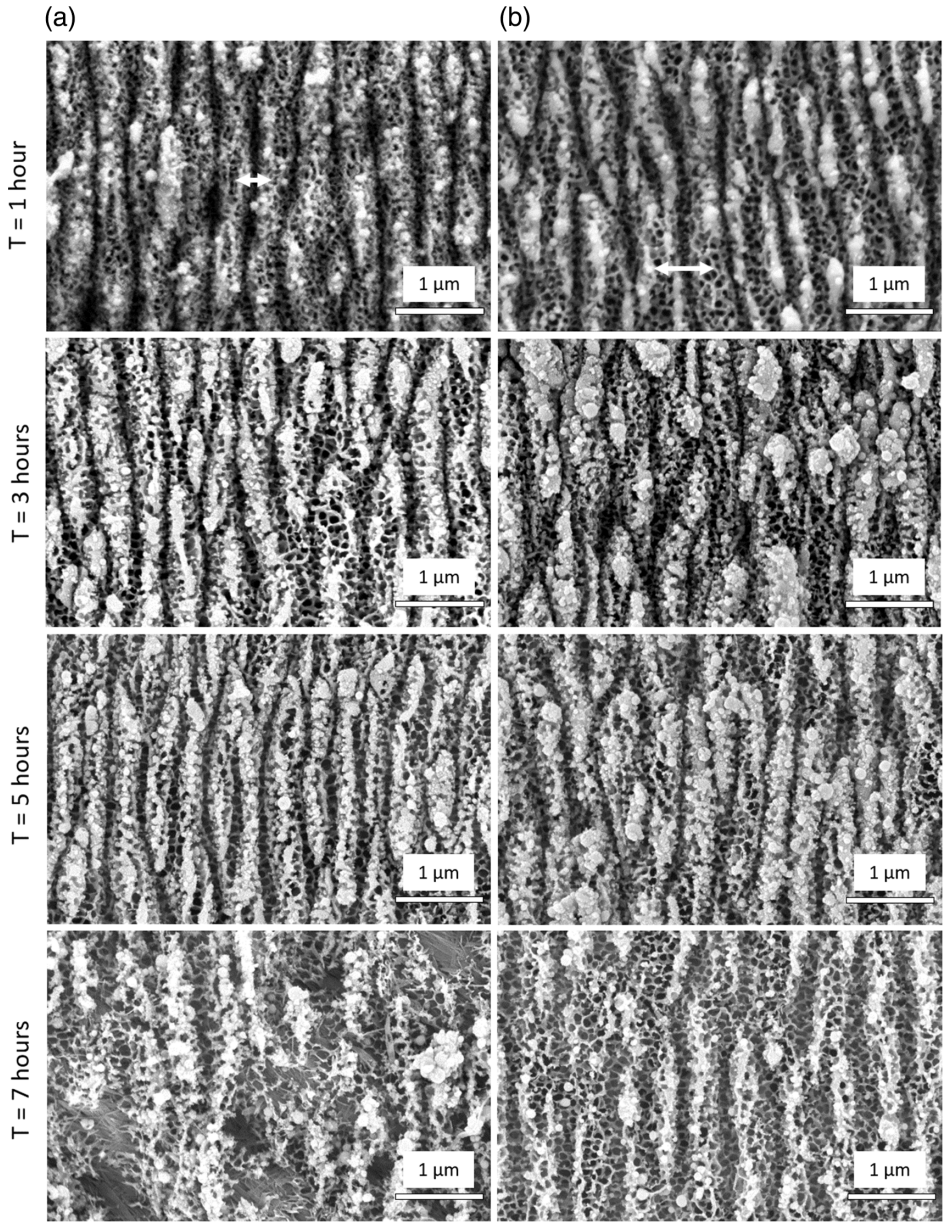

Figure 7. Time evolution of the surface morphology of LIPSS-Sticks at lower magnification for initial LIPSS periods: a) $\lambda_{LIPSS} = 350$ nm and b) $\lambda_{LIPSS} = 500$ nm. Arrows show the enlarged periodicity of the nanotube surface compared with the initial LIPSS spatial period.

the electric potential via: $j = -\sigma \nabla V$, where σ is the conductivity of TiO_2.

We noted in an earlier section that the nanotube diameter in the valley of the LIPSS ripple is larger than at the edge. This can be rationalized by looking at the current density magnitude at the first stage of anodization (Figure 8a). The valley acts as the shortest path from the bottom surface at 60 V to the "ground" at 0 V, hence most of the current density passes through this region. This enhances the electric-field-assisted dissolution process, deepens pores, and enlarges the pore size.[52,53] Therefore, at a later stage of anodization, the pore that is initiated in the valley has a larger diameter and the pores near the crests have a smaller diameter (Figure 8b). However, once further pores are produced, the individual pores have a high current density and continue to deepen. The initial LIPSS ripples are preserved and not etched away, as the current density is low at the surface, thus keeping field-assisted dissolution to a minimum at the top. Furthermore, the oxide nanoparticles created during the initial LIPSS templating process are more abundant on the crests versus the valleys (Figure 5a). Hence, the height of the oxide crest is increased and the current density is expected to be reduced further, although we do not explicitly consider the effect of nanoparticles in the simulation. Additional initial oxide geometries were considered (Section S8, Supporting Information), including a conformally coated oxide, however they fail to reproduce the observed structures.

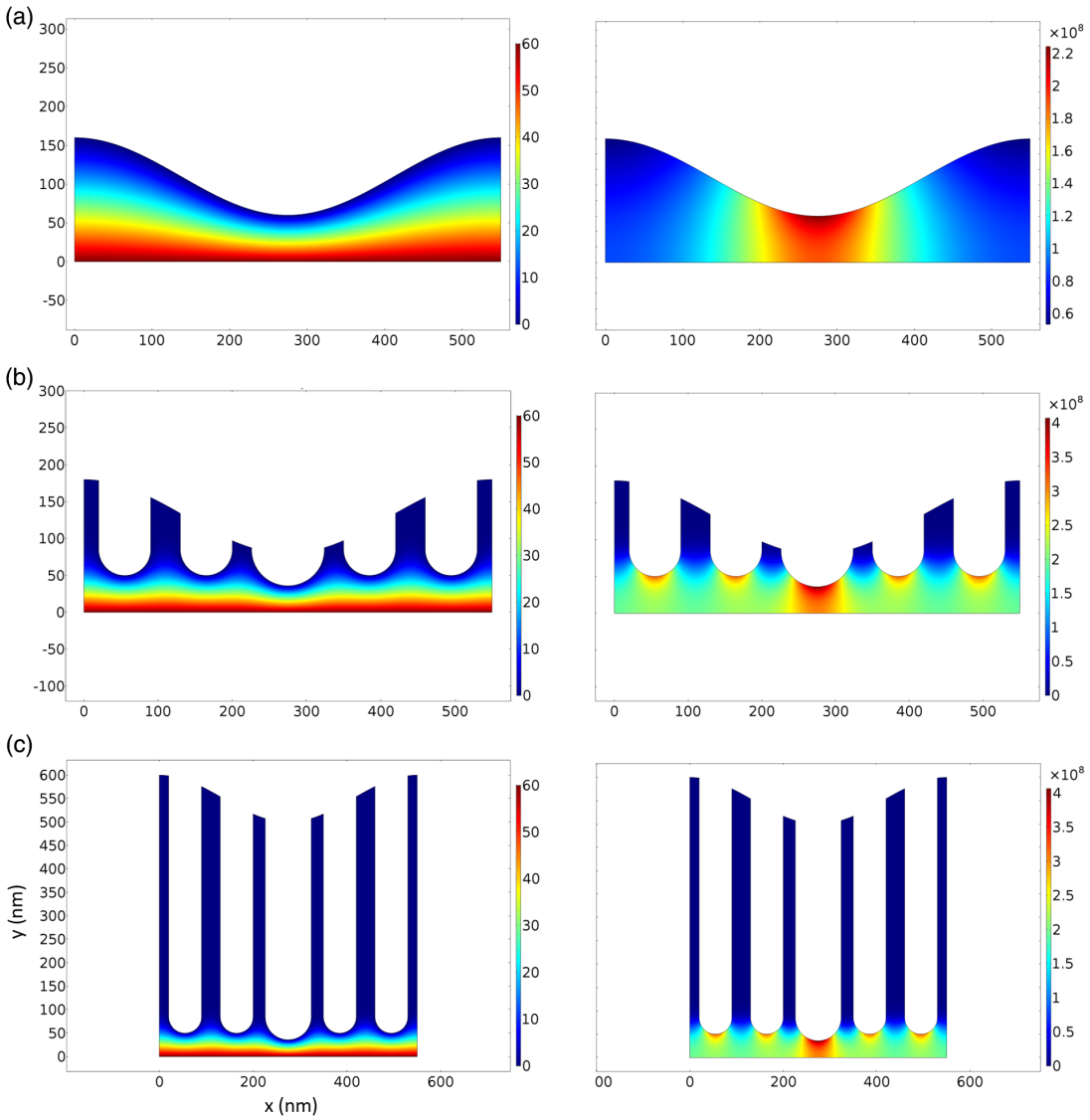

Figure 8. Electrochemical model of the anodization of LIPSS-patterned Ti foil. The *x*–*y* axes are lengths in nm. Left: Electric potential (*V*) map in *V*; Right: Magnitude of current density (||J||) in Am^{-2}. The color bars on the right of each plot indicate the magnitude of the corresponding physical variable. Different stages of anodization: a) Initial LIPSS patterned surface, b) formation of pores, and c) growth of nanotubes.

Our model offers a simple explanation for the nanotube size along the LIPSS ripples, but neglects several key processes and the influence of different initial irregular oxide geometries. We do not consider the diffusion of ions, the evolution of the interface due to stress and overpotential, the oxide electrochemical growth, the etching of the oxide by the fluoride electrolyte, the initial oxide layer formed during laser ablation, and the negative feedback of a time-dependent reduction in current as the oxide film thickens. A more complete model is being developed to consider the effects of the electrolyte and surface stresses evolved in the presence of a laser-templated surface. Despite that, we believe that the qualitative nature of the explanation still holds, because the electric-field strength and electric currents remain the most important contributors to the initial stage of nanotube formation and pore size.[53,54]

3. Conclusion

The novel use of LIPSS on the surface of a metal to template the growth of photocatalytically active TiO_2 nanotube arrays onto a ripple structure is demonstrated. TiO_2 nanotubes are well-known photocatalysts, but have poor visible-light collection efficiency. Approaches such as thermal annealing introduce oxygen vacancy defects and increase the visible-light absorption at the cost of reducing the electron–hole separation lifetimes. The reduced lifetime degrades the photocatalytic efficiency.[13] Ripples/grating-like nanostructures have been shown to enhance the trapping of visible light on materials. We have fabricated structures that have enhanced visible and near-infrared light extinction (Figure 3), which can be understood as a grating scattering effect. More efficient visible-light absorption from

structural enhancement will reduce the amount of oxygen vacancies needed to enhance the visible-light photocatalytic activity.[10,55–57] Hence, the disadvantage of increased electron–hole recombination can be limited while still increasing the visible-light collection efficiency. Furthermore, the grating structure increases the surface area of nanotubes during catalysis, potentially increasing its activity. The photocatalytic and photoelectrochemical properties of these films are under active investigation and will be the subject of future studies.

We also investigated the evolution of the microstructure of TiO_2 nanotubes and attempted to rationalize the nanotube distribution and sizes using computational modeling of the electric field during anodization. The electrostatic model, although limited, is able to explain the relative sizes of the nanotubes between the valleys of the ripple and its crests. Detailed modeling studies will be the subject of future work.

This is a general nanostructure fabrication method, and can be applied to a wide range of transition metal oxides. Electrochemical growth of Cu,[58] Zr,[59] Hf,[60] Ta,[61] Nb,[62] W,[63] Fe,[64] Ti, Ti alloys (TiNb, TiZr, TiW, TiTa),[9] and Al[65] nanotube arrays have been observed, and LIPSS has been shown for Cu,[66] W,[67] Fe,[68] Ti, and Al.[69] Hence the scope for the expansion of this technique is vast, and allows the nanostructure control of metal-oxide electrocatalysts spanning a wide range of redox potentials for different chemical reactions. We anticipate that this approach will be useful for tungsten oxides, where the native oxide's bandgap already lies in the visible regime, and tungsten oxide LIPSS-Sticks should have enhanced light collection efficiency and photocatalytic activity. Furthermore, there are other methods to produce LIPSS, including the use of circularly polarized light to create cross-hatch LIPSS structures.[70] A further application of the nanostructured surface would be to change the wettability of TiO_2 surfaces further using a hierarchy of scales.[71]

4. Experimental Section

Laser Treatment of Ti: Prior to laser treatment, to ensure an even surface to the level of tens of nm surface roughness, Ti foil (0.2 mm thick, 99.96%) was electropolished under 40 V constant voltage in a 1:9 volume ratio perchloric acid:acetic acid. Femtosecond laser treatment (800 nm, 130 fs pulse duration, 1 kHz, Legend Elite, Coherent Inc., USA) was performed on the Ti foil on a micromachining stage (JPSA, Coherent Inc). The fluence was varied between 0.050 and 0.255 J cm^{-2} and the number of pulses overlapped at each point between 1 and 500. The fluence was altered using a matched-polarizer laser power attenuator, and the spot size used for laser treatment was set using a 50 μm × 50 μm metal knife-edge mask in all cases. The number of overlapped pulses was tuned by varying the translation speed of the stage under the laser. For templated electrochemical growth, two fluence-pulse combinations were chosen: 0.105 J cm^{-2}, 250 pulses; and 0.087 J cm^{-2}, 50 pulses, corresponding to laser-induced periodic structures of ≈350 and 500 nm spatial period, respectively. An area of 2 cm × 2 cm was patterned on the electropolished Ti foil prior to electrochemical anodization.

Electrochemical Anodization of Ti: The laser-patterned Ti samples were anodized in an ethylene glycol electrolyte containing 0.25 wt% NH_4F, 2 vol% H_2O for under 60 V constant voltage. The dimensions of the Ti foil used was 5 cm × 4 cm and the working electrode was placed 2 cm away from a Pt counter-electrode. The anodization time was varied at 1, 3, 5, and 7 h to observe the evolution of nanotube morphology. After anodization, the samples were ultrasonicated with ethanol and distilled water and dried at 150 °C to remove organic species.

Surface Characterization: Surface morphology was observed using a desktop SEM (JEOl JCM6000, Coherent), FE-SEM (FEI XL30 S-FEG, Phillips) and optical profilometer (Bruker Contour GTK, Bruker Inc). Cross-section images were obtained by fracturing the brittle TiO_2 layer by delamination or with a razor blade, and tilting it under the SEM. Ultraviolet-visible (Perkin–Elmer) reflectance spectroscopy with an integrating sphere attachment was used to measure the extinction spectrum of the sample, referenced to a $BaSO_4$ standard. XPS was measured with an Axis ultraDLD (Kratos Ltd., UK), using a monochromated Al K-alpha X-ray source (100 W). The chamber pressure was ≈10^{-9} torr and core level scans were measured with a pass energy of 20 eV. The data was fit using CasaXPS (Casa Software Ltd., USA), using Gauss–Lorentzian peaks on a Shirley background. XPS data was referenced to the C1s peak of adventitious surface carbon at 284.8 eV. FTIR spectra was collected with a Nicolet Continuum (Thermo-Fisher Ltd.) with a 40× reflective Cassegrain objective.

Computational Simulations and Image Processing: The electromagnetic spectrum simulations were performed with the computational package GD-Calc,[45] implemented in MATLAB 2016a (Mathworks Inc). The code solves Maxwell's equations on a grating structure using the rigorous coupled wave approximation.[46] All image processing was done with ImageJ.[72] Electrochemical simulations were performed with COMSOL Multiphysics (Comsol Inc), using the AC/DC module.

Supporting Information

Supporting Information is available from the Wiley Online Library or from the author.

Acknowledgements

The authors thank Dr. Catherine Hobbis, Dr. Patrick Conor, and Dr. Marcel Schaefer for aid in SEM measurements, Dr. Colin Doyle and Junzhi Ye for the X-ray photoelectron spectroscopy, and Dr. Wanting Chen and Prof. Geoff Waterhouse for the UV–vis reflectance spectroscopy measurements. The authors also thank Prof. David Williams and Dr. Baptiste Auguie for discussions around the electrochemistry and optical modeling, respectively.

Conflict of Interest

The authors declare no conflict of interest.

Author Contributions

R.A. performed the laser ablation and characterization experiments and wrote the article with W.G. and M.C.S. J.D. performed the electrochemical anodization.

Data Availability Statement

The data that support the findings of this study are available from the corresponding author upon reasonable request.

Keywords

anodization, electrochemistry, laser patterning, laser-induced periodic surface structures, self-organization

Received: November 5, 2020
Revised: January 15, 2021
Published online: March 8, 2021

[1] R. Shi, X. Zhang, G. I. Waterhouse, Y. Zhao, T. Zhang, *Adv. Mater.* **2020**, 2000659.
[2] Y. L. Pang, S. Lim, H. C. Ong, W. T. Chong, *Appl. Catal., A* **2014**, *481*, 127.
[3] M. Ni, M. K. Leung, D. Y. Leung, K. Sumathy, *Renew. Sustain. Energy Rev.* **2007**, *11*, 401.
[4] A. Fujishima, K. Honda, *Nature* **1972**, *238*, 37.
[5] H.-S. Kim, J.-W. Lee, N. Yantara, P. P. Boix, S. A. Kulkarni, S. Mhaisalkar, *Nano Lett.* **2013**, *13*, 2412.
[6] W.-Q. Wu, D. Chen, Y.-B. Cheng, R. A. Caruso, *ACS Appl. Mater. Interfaces* **2020**, *12*, 11450.
[7] F. Huang, D. Chen, X. L. Zhang, R. A. Caruso, Y. B. Cheng, *Adv. Funct. Mater.* **2010**, *20*, 1301.
[8] L. Liu, X. Chen, *Chem. Rev.* **2014**, *114*, 9890.
[9] P. Roy, S. Berger, P. Schmuki, *Angew. Chem., Int. Ed.* **2011**, *50*, 2904.
[10] J. Dong, J. Han, Y. Liu, A. Nakajima, S. Matsushita, S. Wei, W. Gao, *ACS Appl. Mater. Interfaces* **2014**, *6*, 1385.
[11] J. Luo, S. Zhang, M. Sun, L. Yang, S. Luo, J. C. Crittenden, *ACS Nano* **2019**, *13*, 9811.
[12] Y. Zhao, Y. Zhao, R. Shi, B. Wang, G. I. N. Waterhouse, L. Z. Wu, C. H. Tung, T. Zhang, *Adv. Mater.* **2019**, *31*, 1806482.
[13] X. Chen, L. Liu, F. Huang, *Chem. Soc. Rev.* **2015**, *44*, 1861.
[14] M. L. Brongersma, Y. Cui, S. Fan, *Nat. Mater.* **2014**, *13*, 451.
[15] P. Bermel, C. Luo, L. Zeng, L. C. Kimerling, J. D. Joannopoulos, *Opt. Express* **2007**, *15*, 16986.
[16] E. R. Martins, J. Li, Y. Liu, J. Zhou, T. F. Krauss, *Phys. Rev. B* **2012**, *86*, 041404.
[17] S. Schauer, R. Schmager, R. Hünig, K. Ding, U. W. Paetzold, U. Lemmer, M. Worgull, H. Hölscher, G. Gomard, *Opt. Mater. Express* **2018**, *8*, 184.
[18] C. S. Schuster, A. Bozzola, L. C. Andreani, T. F. Krauss, *Opt. Express* **2014**, *22*, A542.
[19] J. M. Macak, H. Tsuchiya, P. Schmuki, *Angew. Chem., Int. Ed.* **2005**, *44*, 2100.
[20] Ö. Ö. Çapraz, P. Shrotriya, P. Skeldon, G. E. Thompson, K. R. Hebert, *Electrochim. Acta* **2015**, *167*, 404.
[21] K. R. Hebert, S. P. Albu, I. Paramasivam, P. Schmuki, *Nat. Mater.* **2012**, *11*, 162.
[22] Q. Ouyang, H. L. Swinney, *Nature* **1991**, *352*, 610.
[23] Q. Dou, P. Shrotriya, W. Li, K. R. Hebert, *Electrochim. Acta* **2019**, *295*, 418.
[24] P. Mishra, K. R. Hebert, *Electrochim. Acta* **2020**, *340*, 135879.
[25] A. Y. Vorobyev, C. Guo, *Laser Photon. Rev.* **2013**, *7*, 385.
[26] J. Bonse, *Nanomaterials* **2020**, *10*, 1950.
[27] J. Bonse, S. Höhm, S. V. Kirner, A. Rosenfeld, J. Krüger, *IEEE J. Select. Topics Quantum Electron.* **2016**, *23*.
[28] J. Bonse, J. Krüger, S. Höhm, A. Rosenfeld, *J. Laser Appl.* **2012**, *24*, 042006.
[29] A. Vorobyev, V. Makin, C. Guo, *J. Appl. Phys.* **2007**, *101*, 034903.
[30] J. Sipe, J. F. Young, J. Preston, H. Van Driel, **1983**, *27*, 1141.
[31] F. Garrelie, J.-P. Colombier, F. Pigeon, S. Tonchev, N. Faure, M. Bounhalli, S. Reynaud, O. Parriaux, *Opt. Express* **2011**, *19*, 9035.
[32] Y. Fuentes-Edfuf, *ACS Omega* **2019**, *4*, 6939.
[33] P. Gregorčič, M. Sedlaček, B. Podgornik, J. Reif, *Appl. Surf. Sci.* **2016**, *387*, 698.
[34] O. Varlamova, F. Costache, J. Reif, M. Bestehorn, *Appl. Surf. Sci.* **2006**, *252*, 4702.
[35] Z. Yu, A. Raman, S. Fan, *Opt. Express* **2010**, *18*, A366.
[36] R. Dewan, D. Knipp, *J. Appl. Phys.* **2009**, *106*, 074901.
[37] K. X. Wang, Z. Yu, V. Liu, Y. Cui, S. Fan, *Nano Lett.* **2012**, *12*, 1616.
[38] S. Bashir, N. Ali, M. S. Rafique, W. Husinsky, C. S. Nathala, S. V. Makarov, N. Begum, *Chinese Phys. B* **2015**, *25*, 018101.
[39] A. Vorobyev, C. Guo, *J. Appl. Phys.* **2015**, *117*, 033103.
[40] J. Bonse, S. Höhm, A. Rosenfeld, J. Krüger, *Appl. Phys. A* **2013**, *110*, 547.
[41] M. Tsukamoto, T. Kawa, T. Shinonaga, P. Chen, A. Nagai, T. Hanawa, *Appl. Phys. A* **2016**, *122*, 1.
[42] B. Nayak, M. Gupta, K. Kolasinski, *Appl. Phys. A* **2008**, *90*, 399.
[43] N. Maharjan, W. Zhou, Y. Zhou, Y. Guan, *Appl. Phys. A* **2018**, *124*, 519.
[44] J. H. Lim, J. Choi, *Small* **2007**, *3*, 1504.
[45] K. C. Johnson, *Grating Diffraction Calculator (GD-Calc®) [Source Code]*, **2019**, https://doi.org/10.24433/CO.7479617.v3.
[46] M. Moharam, T. Gaylord, *JOSA* **1981**, *71*, 811.
[47] S. Sarkar, V. Gupta, M. Kumar, J. Schubert, P. T. Probst, J. Joseph, *ACS Appl. Mater. Interfaces* **2019**, *11*, 13752.
[48] C. A. Grimes, G. K. Mor, *TiO_2 Nanotube Arrays: Synthesis, Properties, and Applications*, Springer Science & Business Media, Berlin, Germany **2009**.
[49] J. Dong, J. Han, W. Qiu, S. Huang, W. Gao, *Scr. Mater.* **2013**, *69*, 374.
[50] C. Cheng, A. Ngan, *Electrochim. Acta* **2011**, *56*, 9998.
[51] L. Stanton, A. Golovin, *Phys. Rev. B* **2009**, *79*, 035414.
[52] G. Singh, A. Golovin, I. Aranson, *Phys. Rev. B* **2006**, *73*, 205422.
[53] Cheng, C.; Ngan, A., in *Nanoporous Alumina*, Springer, New York **2015**; pp 31–60.
[54] Q. Van Overmeere, F. Blaffart, J. Proost, *Electrochem. Commun.* **2010**, *12*, 1174.
[55] X. Chen, D. Zhao, K. Liu, C. Wang, L. Liu, B. Li, Z. Zhang, D. Shen, *ACS Appl. Mater. Interfaces* **2015**, *7*, 16070.
[56] Z. Wang, C. Yang, T. Lin, H. Yin, P. Chen, D. Wan, F. Xu, F. Huang, J. Lin, X. Xie,. *Energy Environ. Sci.* **2013**, *6*, 3007.
[57] J. Nowotny, M. A. Alim, T. Bak, M. A. Idris, M. Ionescu, K. Prince, M. Z. Sahdan, K. Sopian, M. A. M. Teridi, W. Sigmund, *Chem. Soc. Rev.* **2015**, *44*, 8424.
[58] X. Wu, H. Bai, J. Zhang, F. E. Chen, G. Shi, *J. Phys. Chem. B* **2005**, *109*, 22836.
[59] W.-J. Lee, W. H. Smyrl, *Electrochem. Solid-State Lett.* **2005**, *8*, B7.
[60] H. Tsuchiya, P. Schmuki, *Electrochem. Commun.* **2005**, *7*, 49.
[61] N. K. Allam, X. J. Feng, C. A. Grimes, *Chem. Mater.* **2008**, *20*, 6477.
[62] R. L. Karlinsey, *Electrochem. Commun.* **2005**, *7*, 1190.
[63] N. De Tacconi, C. Chenthamarakshan, G. Yogeeswaran, A. Watcharenwong, R. De Zoysa, N. Basit, K. Rajeshwar, *J. Phys. Chem. B* **2006**, *110*, 25347.
[64] R. R. Rangaraju, K. Raja, A. Panday, M. Misra, *Electrochim. Acta* **2010**, *55*, 785.
[65] W. Lee, R. Ji, U. Gösele, K. Nielsch, *Nat. Mater.* **2006**, *5*, 741.
[66] J. Long, P. Fan, M. Zhong, H. Zhang, Y. Xie, C. Lin, *Appl. Surf. Sci.* **2014**, *311*, 461.
[67] A. Vorobyev, C. Guo, *J. Appl. Phys.* **2008**, *104*, 063523.
[68] A. Dauscher, V. Feregotto, P. Cordier, A. Thomy, *Appl. Surf. Sci.* **1996**, *96*, 410.
[69] A. Y. Vorobyev, C. Guo, *Appl. Phys. Lett.* **2008**, *92*, 041914.
[70] G. Lazzini, L. Romoli, F. Tantussi, F. Fuso, *Opt. Laser Technol.* **2018**, *107*, 435.
[71] H. Kang, Y. Liu, H. Lai, X. Yu, Z. Cheng, L. Jiang, *ACS Nano* **2018**, *12*, 1074.
[72] M. D. Abràmoff, P. J. Magalhães, S. J. Ram, *Biophoton. Int.* **2004**, *11*, 36.